Composition, morphology, and optical properties of $CuInSe_2$ thin films electrodeposited using constant and pulsed potentials

M. Valdés & M. Vázquez

Journal of Solid State Electrochemistry
Current Research and Development in Science and Technology

ISSN 1432-8488
Volume 16
Number 12

J Solid State Electrochem (2012)
16:3825-3835
DOI 10.1007/s10008-012-1821-5

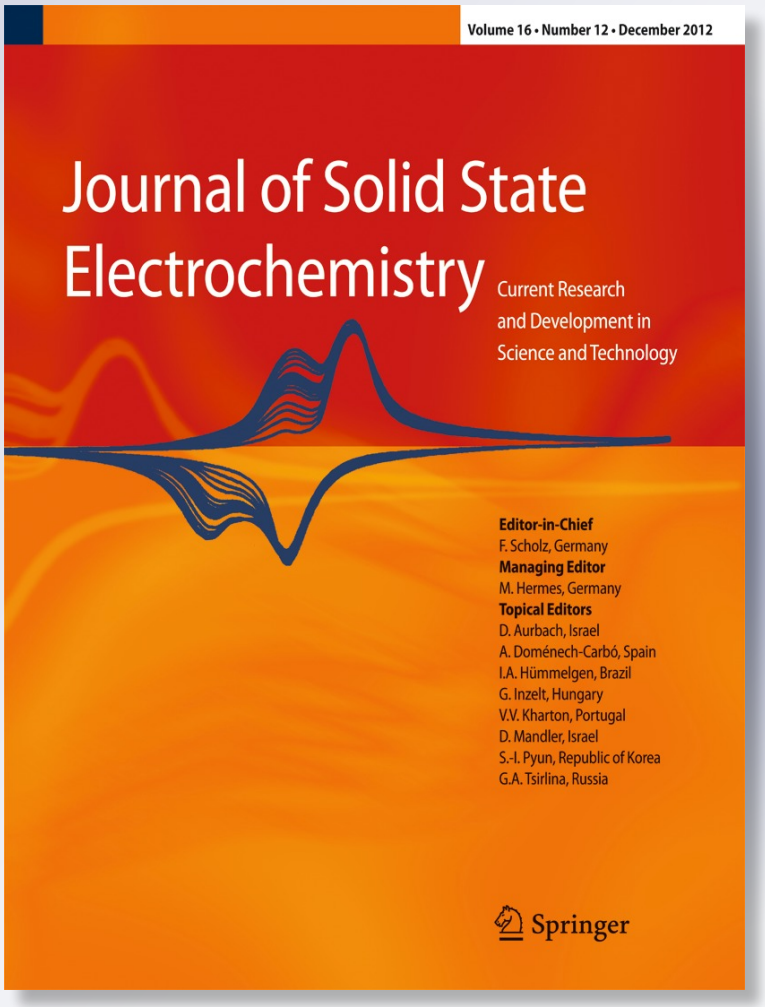

Springer

J Solid State Electrochem (2012) 16:3825–3835
DOI 10.1007/s10008-012-1821-5

ORIGINAL PAPER

Composition, morphology, and optical properties of $CuInSe_2$ thin films electrodeposited using constant and pulsed potentials

M. Valdés · M. Vázquez

Received: 4 December 2011 / Revised: 10 July 2012 / Accepted: 12 July 2012 / Published online: 24 July 2012

Abstract $CuInSe_2$ thin films were electrodeposited on conductive glass using potentiostatic (PoED) and pulsed electrodeposition (PuED). One pulse consisted of a step between two potential values: E_1=−0.9 and E_2=−0.1 V_{SCE}. Each potential was applied during 10 s. Twenty to 180 pulses were applied. In the case of PoED, −0.9 V_{SCE} were applied during 400 to 3,600 s. The differences in crystallographic structure, morphology, and chemical composition between as-deposited PoED and PuED films were investigated by X-ray diffraction, Raman spectroscopy, scanning electron microscopy, and energy dispersive scanning spectroscopy. The presence of secondary phases seemed to be reduced by using PuED. X-ray diffraction showed no significant differences between films prepared by PuED and PoED. Instead, micro-Raman spectroscopy revealed that the chemical composition and homogeneity were improved by pulsing the potential. The thickness of the films increased, and the crystallinity improved as more pulses were applied. For both types of electrodeposition, longer times favored the formation of nearly stoichiometric $CuInSe_2$. For the electrical characterization, the films were annealed in argon and then etched in a KCN solution. KCN etching showed no effect in the film composition. Photoelectrochemical tests and I–V curves confirm p-type conduction. The differences observed in composition, morphology, and optoelectronic properties were attributed to the current profile imposed on the electrode.

Keywords Chalcogenides · Semiconductors · Chemical synthesis · Raman spectroscopy

M. Valdés (✉) · M. Vázquez
División Electroquímica y Corrosión, INTEMA,
Facultad de Ingeniería,
CONICET-Universidad Nacional de Mar del Plata,
Juan B. Justo 4302,
B7608FDQ, Mar del Plata, Argentina
e-mail: mvaldes@fi.mdp.edu.ar

Introduction

$CuInSe_2$ is one of the most extensively investigated materials in the field of thin film solar cells. However, highly efficient solar cells that employ $CuInSe_2$ or its related quaternary alloy $Cu(Ga,In)Se_2$ involve expensive vacuum-based processes. Cost-reduction can be achieved by carefully choosing the deposition techniques used to prepare each layer of the solar cell. Among them, electrodeposition presents important advantages: It can produce large area coatings; it can copy intricate geometries, and it can be used even on top of flexible substrates [1, 2]. In particular, pulsed electrodeposition is a promising method that could be used to infiltrate nanostructured substrates [3, 4]. Structures that are interpenetrated on the nanoscale could constitute an interesting alternative to prepare solid 3D solar cells, with extensive contact between the semiconductor materials [5].

It should also be taken into account that there are some disadvantages associated to the electrodeposition method. In the particular case of the Cu-In-Se ternary system, a well-known drawback is the generation of secondary phases, such as Cu_xSe, which is usually solved by etching with KCN solutions [6–8]. Recently, other authors have demonstrated that a three-potential pulse electrodeposition can be used to produce $CuInSe_2$ films on ITO substrates with an improved morphology, reducing the number of agglomerates and producing a more uniform grain size [9]. It is also well known that the crystallinity of the films needs to be improved by carrying out thermal treatments. But given that Se vaporizes at temperatures higher than 220 °C, the films annealed in vacuum or inert atmospheres usually present high levels of Se vacancies. For this reason, the replacement of the lost selenium has to be taken into account choosing an appropriated atmosphere for the thermal treatments [1, 10]. Also, the high toxicity of most of

the Se sources used during annealing can be a limitation for mass production of $CuInSe_2$ devices. So, even when there are well-known and efficient measures to compensate for the drawbacks, most of them impose serious environmental issues and increase costs.

In our previous work [11], we evaluate the influence of the deposition potential when using potentiostatic (PoED) and pulsed electrodeposition (PuED). This new investigation is focused on the influence of the current profile imposed on the electrode. In particular, the objective is to obtain $CuInSe_2$ films free of secondary phases (such as Cu_xSe) and to minimize the need of the KCN etching to remove them. The changes in structure, morphology, and composition produced when the potential is pulsed are evidenced by comparison with $CuInSe_2$ thin films electrodeposited at constant potential. In the next stage of this investigation, the viability of infiltrating nanostructures of TiO_2 with $CuInSe_2$ produced by pulsed electrodeposition will be explored.

Experimental section

$CuInSe_2$ was electrodeposited from a single bath. Glass coated with fluorine-doped tin oxide was used as substrate (FTO, Libbey Owens Ford, ~8 Ω/sq). The substrate was cleaned thoroughly and rinsed as described earlier [12]. The electroactive area was 1.13 cm^2.

A three-electrode cell, with a Pt mesh as counter electrode and a saturated calomel electrode (SCE) as reference electrode, was used. The electrodeposition was performed employing a PGP 201 Voltalab potentiostat/galvanostat.

PoED was carried out holding the potential at −0.9 V_{SCE} during a given time, between 400 and 3,600 s. The solution was purged with nitrogen to remove dissolved oxygen before starting the electrodeposition. After completing the electrodeposition, the samples were rinsed with distilled water and dried in air.

When using PuED, one pulse consisted of applying −0.9 V_{SCE} for 10 s and then −0.1 V_{SCE} for the next 10 s [13]. To produce $CuInSe_2$ films with different thicknesses, 20 to 180 pulses were applied, taking from 400 to 3,600 s.

Both in the case of PoED and PuED, the precursor electrolyte was an aqueous solution containing 2.5 mmol L^{-1} $CuCl_2$, 10 mmol L^{-1} $InCl_3$, and 5 mmol L^{-1} SeO_2 with 0.2 mol L^{-1} KCl as supporting electrolyte (Cu/In/Se ratio results in 1:4:2). The pH was adjusted between 2 and 2.5 with a few drops of a concentrated HCl stock solution.

$CuInSe_2$ films were annealed in argon at 500 °C during 30 min, using a home-built reactor. After annealing, some films were chemically etched by a 5-min immersion in KCN solution (0.5 mol L^{-1}) to elucidate the effect of the chemical attack on the composition of the films.

The crystalline structure of the films was analyzed by X-ray diffraction in grazing incidence configuration (GXRD, 3° incidence angle) using a PANalytical X'Pert PRO diffraction system employing CuKα radiation at 40 kV and 40 mA. The samples were scanned between 15° and 75° with a step size of 0.01°. GXRD data were analyzed using X'Pert PRO HighScore software, and the crystallographic data for each phase were taken from the literature [14].

Raman spectroscopy measurements were performed using an Invia Reflex confocal Raman microprobe using a ×50 objective. Excitation was provided with the 514 nm emission line of an Ar^+ laser. The Raman spot is circular (diameter ~1 μm). Using neutral density filters, the power of the laser was reduced to 10 % to prevent damage by heating. In this configuration, the laser power on the sample was 0.2 mW, as measured with a silicon photodiode (Coherent Inc.). For this power level, no thermal damage was observed. Raman micro-mapping was performed by recording 29 spectra along the diagonal of 20×20-μm squares. Raman spectra were taken averaging three acquisitions of 20 s each.

A scanning electron microscope (JEOL JSM-6460LV) coupled with an X-ray energy dispersive spectroscopy analyzer (EDAX Genesis XM4-Sys 60 Multichannel Analyzer) was used to study the film morphology and composition.

A Shimadzu UV-160A spectrophotometer was employed to register absorption spectra in the wavelength range 350–1,100 nm at room temperature and to calculate the band gap energy (E_{gap}) by extrapolation.

Photocurrent and current–voltage measurements were carried out forming a semiconductor/electrolyte junction by immersion of the FTO/$CuInSe_2$ film in 0.1 mol L^{-1} Na_2SO_4 solutions. The light beam entered into the cell through a quartz window and shined on the film side of the glass used as substrate. In the case of the photocurrent evaluation, the light source was a solar simulator coupled with an air-mass filter 1.5 G (Oriel-Newport 96000). The light was chopped using an electronic shutter (Uniblitz model T132). To register the I–V curves, the light source was a 150 W Xe lamp, coupled to a filter to remove the ultraviolet radiation. An IVIUM compact potentiostat was employed to carry out these measurements.

Results and discussion

The evolution of the potential in time and the corresponding response in current density (J) for both types of electrodeposition (PoED and PuED) are compared in Fig. 1a and b, respectively. From Fig. 1a, a noticeable current drop is evident as soon as the potential is imposed. This is related to a fast reduction of the ions that are near the electrode surface. After the initial 100 s, a limiting current is recorded, typical of a deposition process controlled by mass transport.

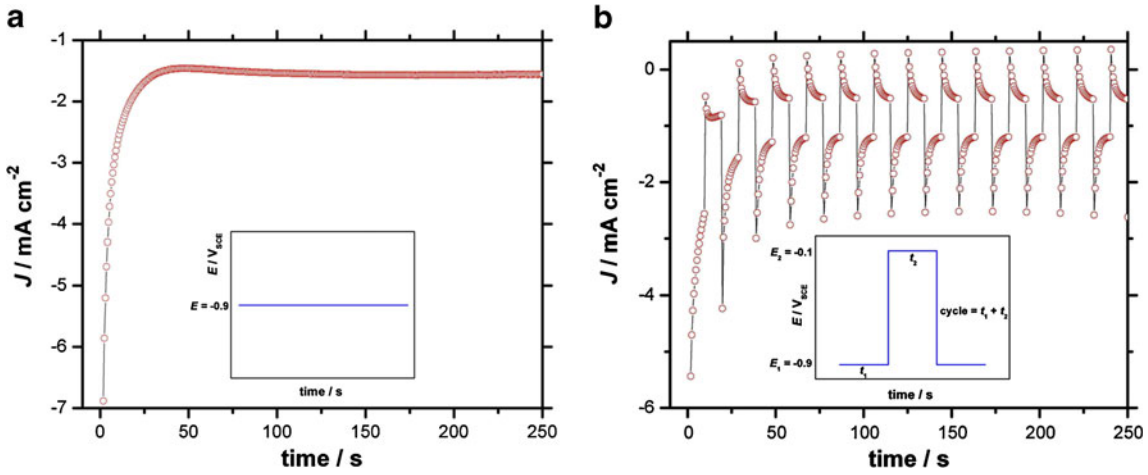

Fig. 1 Potential–time profile imposed during the deposition of $CuInSe_2$ films and the corresponding current–time response. **a** PoED; **b** PuED

PuED (Fig. 1b) presents a more complex current–time response. It can be seen that, when the potential E_1 (or "negative potential") is applied, the current increases sharply and then decreases tending to a steady value, similar to what is observed in PoED. However, when potential E_2 (or "positive potential") is applied, the current drops even more. During this period, ions migrate to depleted areas in the bath. When E_1 is applied again, more evenly distributed ions are available for deposition onto the substrate [15]. Furthermore, starting from the third cycle anodic currents are recorded right after imposing E_2. In addition to replenishing the diffusion layer, these short periods when the current is anodic may contribute in selectively dissolving impurities or secondary phases to produce a more uniform deposit. The differences observed between Fig. 1a and b may provide an explanation for morphological heterogeneity to be illustrated in Fig. 2.

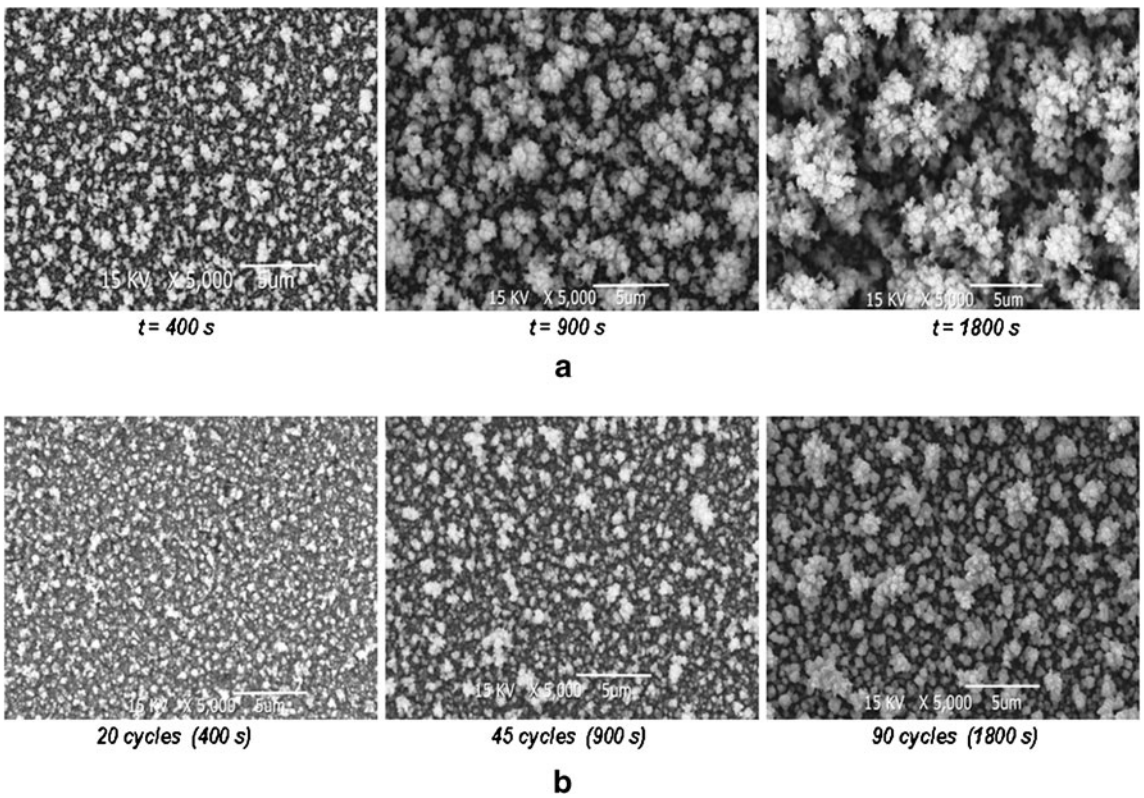

Fig. 2 Scanning electron microscopy (SEM) images of as-deposited samples prepared at −0.9 V_{SCE}, using various times and number of pulses, as indicated. **a** PoED and **b** PuED. The scale *bar* denotes 5 μm in every picture

The current profiles shown in Fig. 1a and b can also be used to calculate the thickness of the films (T), by means of an equation based on Faraday's law (Eq. 1):

$$T = \frac{1}{nF}\left(\frac{JtM}{\rho}\right) = \frac{1}{nF}\left(\frac{QM}{\rho}\right) \quad (1)$$

Here, n is the number of electrons transferred, F is Faraday's number, J is the current density, t is the deposition time, M is the formula weight, and ρ is the density. The total charge Q was calculated by the integration of the $J(t)$ curves recorded in each deposition. In the case of $CuInSe_2$, M= 336.28 g/mol and ρ=5.77 g/cm^3 [16]. Also, 13 electrons are exchanged, as described by reaction (2):

$$Cu^{+2} + In^{+3} + 2SeO_3^{-2} + 12H^+ + 13e^- \rightarrow CuInSe_2 + 6H_2O \quad (2)$$

As it can be seen in Table 1, the thickness of the films increased with the number of pulses applied. Average values of over three individual experiments were calculated.

Figure 2 displays scanning electron microscopy (SEM) images of as-deposited samples, where PoED and PuED are compared. The films grown at constant potential turned out to be very porous, presenting a cauliflower-like structure frequently found for electrodeposited $CuInSe_2$ films [17–19]. This type of morphology became more characteristic at longer deposition times, which is most likely associated to a deposition process controlled by mass transport. The films prepared by pulsed electrodeposition are also porous. However, these films exhibited a more compact and homogenous coverage, with submicron-size grains.

For films grown with 90 or more pulses, the thickness showed good agreement with the values determined from SEM cross-section images. As these films are porous, this demonstrates that the efficiency of electrodeposition is below 100 %. For this reason and since that the formula weight and density vary with the sample composition, Eq. 1 should be taken as an approximation. Applying fewer pulses, the films were found to be so thin that thickness evaluation by SEM was not possible. Furthermore, as expected, PoED produced thicker films for equivalent total times, since the negative potential is effectively applied during the whole period of time.

Table 1 Average thicknesses of electrodeposited $CuInSe_2$ films calculated using Faraday's law (Eq. 1) and assuming 100 % efficiency in the electrodeposition process

Number of pulses	Thickness, μm	Deposition time, s	Thickness, μm
20	0.14	400	0.23
40	0.31	900	0.64
90	0.70	1,800	1.02
180	1.00	3,600	2.64

Figure 3 presents GXRD diffractograms of $CuInSe_2$ films supported on FTO substrates. The low-intensity peaks are magnified in an inset in each figure. The films were electrodeposited using constant and pulsed potentials (Fig. 3a and b, respectively). The substrate diffraction pattern is included in both figures for the sake of comparison, which also shows some peaks that can be attributed to the CuKβ radiation from the X-rays that cannot be filtered due to the incidence angle. Unfortunately, the main diffraction plane of $CuInSe_2$ (112) appears at almost the same angle than the most intense peaks from SnO_2 (main component of FTO). This difference is less than 0.1°.

As it can be seen in Fig. 3a, those films prepared using PoED do not show any of the diffraction planes typical of the $CuInSe_2$ chalcopyrite phase (PDF no. 40–1487), independently of the deposition time. Most of the peaks in the diffractogram are attributed to the substrate (SnO_2, PDF no. 77–0452). This can be taken as an indication of the low degree of crystallinity, which is usual in as-deposited samples of this material. At 400 s, low-intensity peaks related to metallic indium (PDF no. 01–1042) and CuIn (PDF no. 35–1150) alloys can be identified. At longer times, additional diffraction peaks corresponding to In_2Se_3 (PDF no. 72–1469) and $Cu_{11}In_9$ (PDF no. 41–0883) are identified, revealing that as-deposited PoED films contain an excess in indium. This was further confirmed by energy dispersive spectroscopy (EDS) (see below). The presence of In_2Se_3 and CuIn alloys in electrodeposited $CuInSe_2$ films has been reported before by other authors [20, 21]. In the case of the films obtained by PuED (see Fig. 3b), 20 pulses most likely produce an extremely thin film where only diffraction peaks from the substrate can be identified. After more pulses were applied, particularly using 90 pulses, new diffraction peaks are present. Among them, there is a broad signal around 44.5° that can be assigned to the diffraction of the characteristic trigonal plane splitting (204/220) of the $CuInSe_2$ phase. Alternatively, it can be related to the diffraction of $Cu_{1.8}Se$ (PDF no. 71–0044).

After annealing at 500 °C during 30 min, the crystallinity and phase composition of the films changed significantly. In the case of PoEd films (Fig. 3c), the films electrodeposited during 900 s present several peaks that can be attributed to In_2S_3 (PDF no. 12–0117). No diffraction peaks related to $CuInSe_2$ tetragonal phase could be identified. As it was observed in as-deposited PoED films, the high indium content obtained at this potential promotes the formation of binary indium compounds. Using longer deposition times (1,800 s), the results are similar, but, instead of indium selenide, the films present peaks characteristic of In_2O_3 (PDF no. 74–1990). This could be the result of partial oxidation during thermal treatment. Despite this, other peaks

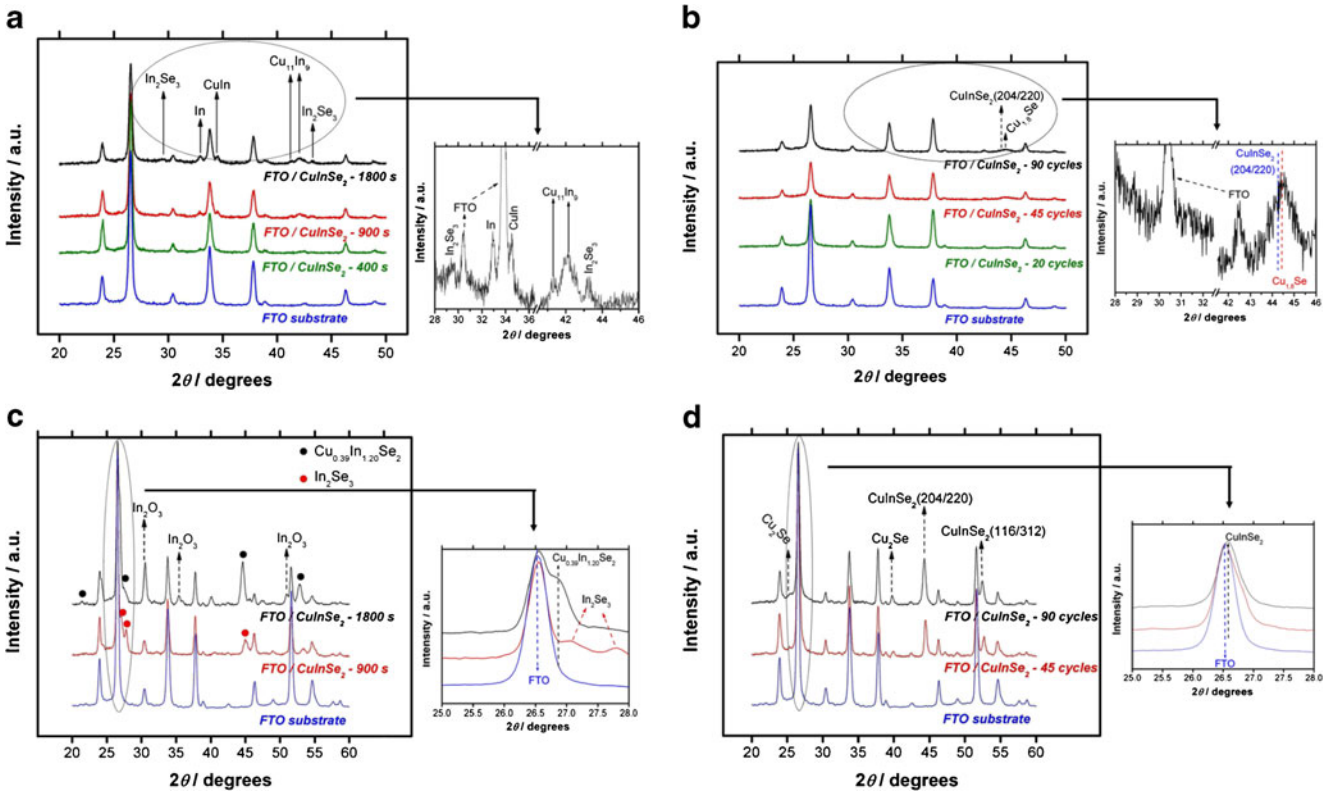

Fig. 3 GXRD diffractogram of $CuInSe_2$ films deposited using different number of pulses and times. **a** As-deposited PoED; **b** as-deposited PuED; **c** annealed PoED, and **d** annealed PuED. The *inset* in each figure is provided to clarify the analysis

could be assigned to an indium-rich chalcopyrite phase such as $Cu_{0.39}In_{1.20}Se_2$ (PDF no. 42–0862). A zoom within 25° to 28° provides more details regarding the difference in phase composition between these films and the substrate. The high indium content in as-deposited films (see EDS results, Table 2) can explain these stoichiometry deviations in these films and the presence of indium binary compounds as In_2S_3 and In_2O_3.

Annealed PuEd films (Fig. 3d) show diffraction peaks typical of tetragonal $CuInSe_2$ (PDF no. 40–1487). Additional signals can be associated to Cu_2Se compounds (PDF no. 19–0401) that are frequently formed in $CuInSe_2$ deposition [6, 22]. PuED films prepared at different number of cycles do not show significant difference in their crystal structure, in contrast with the case of PoED films (Fig. 3c). Again, Fig. 3d includes a zoom between 25° and 28°. In this case, it can be seen that, as the number of cycles increases, the peak maximum gets closer to the position of the (112) $CuInSe_2$ plane and can be easily identified from the contribution of the FTO substrate.

Table 2 presents the composition of as-deposited samples as a function of the number of pulses applied or the time used, as determined by energy dispersive X-ray spectroscopy. Those samples prepared by PoED present a noticeable excess in the content of indium, as was discussed above in relation to XRD results. Only after 1 h of deposition is the global composition close to that of the stoichiometric

Table 2 Chemical composition of as-deposited $CuInSe_2$ thin films determined by EDS

PuED						PoED					
Number of pulses	Cu	In	Se	Cu/In	Se/(Cu+In)	Time, s	Cu	In	Se	Cu/In	Se/(Cu+In)
20	22.1	15.9	62.0	1.4	1.6	400	19.9	29.9	50.2	0.7	1
45	24.2	17.6	58.2	1.4	1.4	900	21.2	42.9	35,9	0.5	0.5
90	20.7	21.1	58.2	0.9	1.4	1800	21.4	48.9	29.7	0.4	0.4
180	27.1	25.2	47.7	1.1	0.9	3600	26.1	24.5	49.4	1.1	1.0

PuEd pulse electrodeposition, *PuEd* potentiostatic electrodeposition

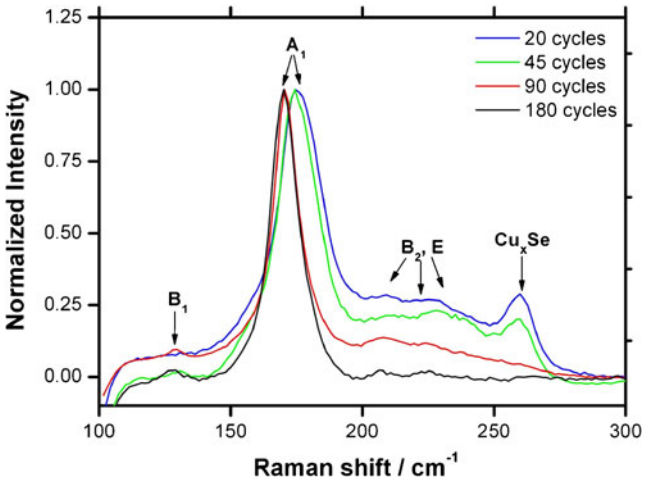

Fig. 4 Raman spectra of samples prepared by PuED with different number of pulses (20 to 180)

formula ($Cu_{1,07}In_{0.95}Se_{1.98}$). It has to be taken into account that, when using PoED the applied potential might be too negative, since the electrodeposition on metallic substrates is generally done imposing potential from −0.4 to −0.8 V_{SCE}.

When using PuED, the evolution in the indium and selenium contents as the number of pulses increased (see Table 2) is more regular. The amount of indium increases and that of selenium decreases, while the content in copper remains mostly constant as more cycles are applied. Low indium contents for 20 and 45 pulses could be indicating that, at short times, the film is mainly composed by Cu_xSe. It has been demonstrated that the formation of $CuInSe_2$ proceeds via the initial deposition of Cu_xSe which later reacts with the indium present in the solution [22, 23]. In contrast, EDS results show that after applying 180 pulses, a film with a composition that is close to the stoichiometric formula was obtained. These results will be complemented with those from Raman spectroscopy, to be described below.

Figure 4 presents average Raman spectra of samples prepared by PuED at −0.9 V_{SCE} with different number of pulses (20 to 180). Table 3 presents the position of the peaks together with FWMH values (full width at half maximum) for the A_1 mode peaks shown in Fig. 4. All the spectra contained the A_1 mode within 170–175 cm^{-1} related to the vibration of Se–Se bonds (anions), but this signal was sharper and more intense in films grown with higher number of pulses (90–180), typical of more crystalline films [24, 25].

Table 3 Position of the A_1 mode Raman peaks in Fig. 4 and full width at half maximum values (FWMH)

Number of cycles	A_1 position, cm^{-1}	FWHM, cm^{-1}
20	178.64	16.07
45	177.13	15.36
90	174.37	9.97
180	173.32	12.94

The position of the peaks of $CuInSe_2$ films deposited with fewer pulses (20–45) was blue-shifted with respect to the position of the A_1 mode. This can be related to residual stress or to a higher density of defects present in these films [25]. The spectra of films deposited with 20 and 45 pulses (see Fig. 4) shows a small shoulder at 259 cm^{-1} that can be attributed to Cu_xSe produced during the first stages of $CuInSe_2$ formation [26, 27]. Using more pulses, this signal can no longer be seen, indicating reaction with In^{+3} ions when given enough time. Additional vibration modes typical of chalcopyrite are also present in the spectra of the films deposited with 90 and 180 pulses [28]. At 128 cm^{-1}, the B_1 mode assigned to the vibration of Cu-In bonds and the low-intensity band B_2,E between 200 and 230 cm^{-1} are present.

In order to check the compositional homogeneity of the samples, Raman micro-mapping was performed by recording 29 spectra along the diagonal of 20×20-μm regions. Figure 5 presents the optical image obtained with the Raman microscope used for the micro-mapping analysis.

Figure 6a displays Raman mapping of $CuInSe_2$ films prepared by PuED using different numbers of pulses. All the samples show good spatial homogeneity. It can also be confirmed that the A_1 mode is the most intense signal in every spectrum, even in the sample prepared with only 20 pulses. However, the film obtained using 20 pulses shows a significant contribution of the Cu_xSe binary phase, extended all over the sample. When using more pulses, the bands due to binary phases present lower intensities and are randomly distributed throughout the mapped zone. This confirms that

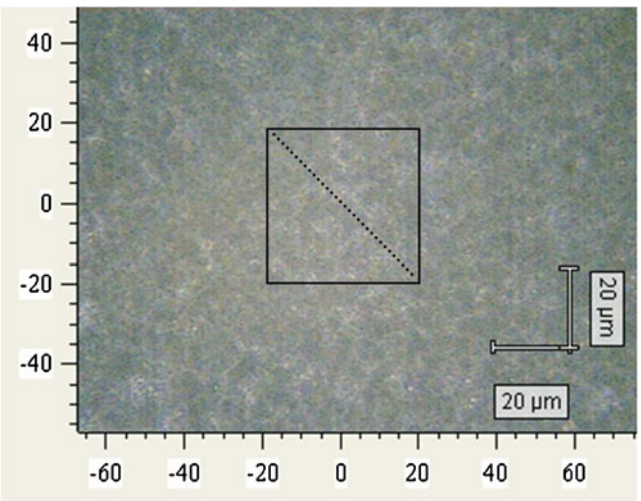

Fig. 5 Optical image of a $CuInSe_2$ film showing details of the procedure used for Raman micro-mapping analysis

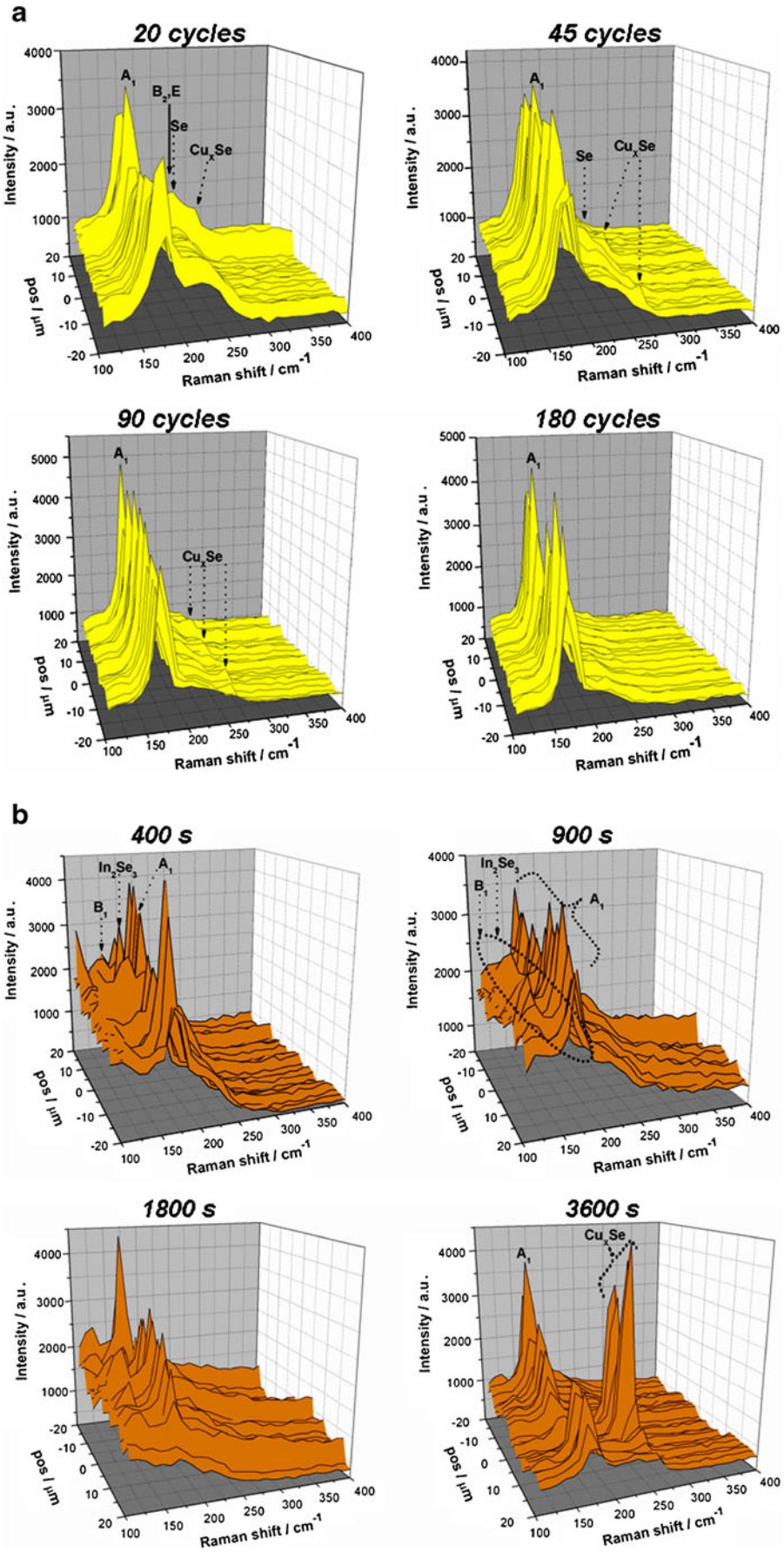

Fig. 6 Micro-Raman mapping performed on as-deposited $CuInSe_2$ films prepared at −0.9 V_{SCE} using **a** PuED at different number of pulses (20 to 180) and **b** PoED at different deposition times (400 to 3,600 s)

the indium incorporation by reaction with Cu_xSe is the mechanism that ultimately leads to the formation of $CuInSe_2$. With 90 pulses, the homogeneity of the film is notorious, with the mode A_1 evenly distributed along the whole mapped area. Remnant Cu_xSe small signals are still present. When the deposition time is duplicated (180 pulses), these signals seem to be absent, and $CuInSe_2$ is the only phase in the film. In agreement with the results presented in Table 4, this is an important result taking into account the benefits of avoiding the use of toxic KCN as etchant to eliminate residual Cu_xSe.

Figure 6b presents an equivalent set of maps for $CuInSe_2$ films obtained using potentiostatic electrodeposition (PoED) at different times. As in Fig. 6a, the results show that $CuInSe_2$ is the main phase present. In contrast, this signal is not as evenly distributed as in those films obtained by pulsing the potential (PuED films). At lower deposition times (400 s), the indium in excess, previously seen, is also evident in the Raman maps, with a signal at 144 cm^{-1} which can be assigned to γ-In_2Se_3 [29, 30]. Another vibration mode present in these maps is the B_1 produced by Cu-In bonds. This mode is not present in PuED films maps, which suggests that it is related to an In-rich film. At longer deposition times (900 and 1,800 s), the signals from γ-In_2Se_3 are absent in the spectra. As it was previously observed by EDS analysis, the composition of the film deposited during 3,600 s is close to stoichiometric $CuInSe_2$. However, the Raman map shows that, besides $CuInSe_2$, there are zones along the film where binary Cu_xSe is the predominant phase, as indicated by the intense signals around 260 cm^{-1}.

From the comparative analysis of Fig. 6a and b, it can be deduced that pulsed electrodeposition produces films of better structural and compositional homogeneity with a lower participation of residual binary compounds.

Table 5 presents a comparative summary of the phase and composition analysis performed using GXRD and micro Raman spectroscopy. GXRD provides an interesting contrast of phase composition between PoEd and PuEd as deposited $CuInSe_2$ films, as was discussed previously. Unfortunately, differences in the composition of the films obtained at different times or cycles could not be detected by GXRD. This is probably due to the low crystallinity of the films. It is well known that Raman spectroscopy has a higher level of sensitivity for surface material analysis. So, the differences in phase composition for the various experimental conditions being tested are more easily detected by Raman spectroscopy.

Table 4 Chemical composition of $CuInSe_2$ films determined by EDS (effect of post-treatments)

PuED, 90 cycles	Cu	In	Se	Cu/In	Se/(Cu+In)
As-deposited	20.7	21.0	58.2	1.0	1.4
Annealed	22.6	21.9	55.5	1.0	1.2
KCN etching/2 min	23.3	21.8	54.9	1.1	1.2
KCN etching/5 min	23.4	22.0	54.7	1.1	1.2

The influence of annealing is analyzed in Fig. 7, where Fig. 7a shows spectra recorded at random spots on as-deposited samples prepared by PuED (E_1=−0,9 V_{SCE} and 90 pulses). These are compared with other group of spectra in Fig. 7b, recorded on samples annealed at 500 °C in argon. It can be seen that as-deposited $CuInSe_2$ films (Fig. 7a) show broad and low-intensity signals, characteristic of the $CuInSe_2$ vibration modes. Additional Raman signals, at 240 and 260 cm^{-1}, can be attributed to trigonal selenium and Cu_xSe compounds, respectively [31]. The formation of this Se in excess (also evidenced by EDS analysis) could be related to the higher current densities reached when pulsing the potential, which favor the deposition of the element with the most noble electrochemical reduction potential. Some authors argue that the presence of Se in excess can also enhance the formation of Cu_xSe in the film [17, 32].

After annealing, a clear increment in the intensity and sharpness of the $CuInSe_2$ A_1 Raman mode can be observed, showing the well-known beneficial effect of the thermal treatment, which improves crystallinity and composition. Moreover, the relative intensities of the various signals in each spectrum are in agreement with Raman analysis performed on $CuInSe_2$ obtained by other authors using high-vacuum and high-temperature techniques [33, 34]. The band attributed to trigonal Se is less intense when the annealed films are analyzed. This confirms that the remnant Se is partially vaporized during the annealing stage. It is also possible that, during the thermal treatment, the reaction between secondary phases is enhanced, and more $CuInSe_2$ is formed, with the consequent decrease in the amount of trigonal Se.

The effect of annealing and KCN etching were also analyzed by EDS and are shown in Table 4. In agreement with previous results, the annealing stage seems to improve the stoichiometry of the $CuInSe_2$ layer by reducing the amount of Se, even though the annealed samples are still rich in Se. Reducing the Se concentration in the precursor electrolyte or annealing over longer times could be suitable strategies to adjust the Se content in the case of films prepared by pulsed electrodeposition. Instead, etching shows no further improvement in the average composition of the film.

The band gap energy values (E_{gap}) of semiconductor films were determined from transmittance spectra by

Table 5 GXRD and Raman spectroscopy-phase analysis summary for as-deposited PoED and PuEd $CuInSe_2$ films

Deposition	Time	GXRD	Raman spectroscopy
PoEd	400 s	In, CuIn	In-Cu (modes), In_2Se_3, $CuInSe_2$
	900 s	In, In_2Se_3, CuIn, $Cu_{11}In_9$	In-Cu (modes), In_2Se_3, $CuInSe_2$
	1,800 s	In, In_2Se_3, CuIn, $Cu_{11}In_9$	In-Cu (modes), In_2Se_3, $CuInSe_2$
	3,600 s	–	$CuInSe_2$, Cu_xSe
PuEd	20 cycles	(only FTO)	Se, Cu_xSe, $CuInSe_2$
	45 cycles	(only FTO)	Se, Cu_xSe, $CuInSe_2$
	90 cycles	$Cu_{1.8}Se$, $CuInSe_2$	Cu_xSe, $CuInSe_2$
	180 cycles	–	$CuInSe_2$

plotting $(-\ln(T)h\nu)^2$ versus $(h\nu)$ and are shown in Fig. 8 for samples prepared using 20 to 180 pulses, after the annealing treatment. The calculated E_{gap} values vary between 0.9 and 1 eV, in close agreement with values reported for $CuInSe_2$ films obtained by three-potential pulsed electrodeposition [9] and by fixed potential deposition [35, 36]. The differences in the bang gap energy values may be attributed to variations in the chemical composition between both types of films. Other authors have found a similar behavior in $CuInSe_2$ films having different Cu/In ratios which were prepared by spray pyrolysis [37].

Given that n-type and p-type $CuInSe_2$ have been prepared by electrodeposition before [38], photoelectrochemistry was used to explore the nature of the carriers. A negative photocurrent is registered when photoproduced electrons move across the space charge region toward the electrode/electrolyte interface and increase the cathodic current [39]. Figure 9 shows the photocurrent registered at open circuit potential, comparing films prepared at constant and pulsed potential. In both cases, the p-type character of the film could be confirmed by recording negative photocurrent. The photocurrent attains more than two times higher values when the $CuInSe_2$ is prepared using pulsed electrodeposition. Furthermore, the thickness of the PuED film is lower than the PoEd layer (see Table 1), which means that the light absorption is reduced and so too the carrier generation This can be taken as an evidence of the superior quality of the $CuInSe_2$ film obtained using pulsed electrodeposition.

The potentiodynamic I–V curves, in the dark and under illumination, are shown in Fig. 10. The dark current density J_d is relatively small, but upon irradiation, the curve exhibits a cathodic photocurrent J_{ph}, supporting the p-type conduction. The onset of the photocurrent can be correlated to the flat band potential (E_{fb}) according to the relation $J_{ph} \propto (V_{fb}-V)$ [39]. So, the flat band potential can be estimated, and for $CuInSe_2$ films in contact with Na_2SO_4 solution, it results that $E_{fb}=-0.58$ V.

Conclusions

$CuInSe_2$ films were electrodeposited onto FTO glass from a single bath and using two-step potential pulses. 20 to 180

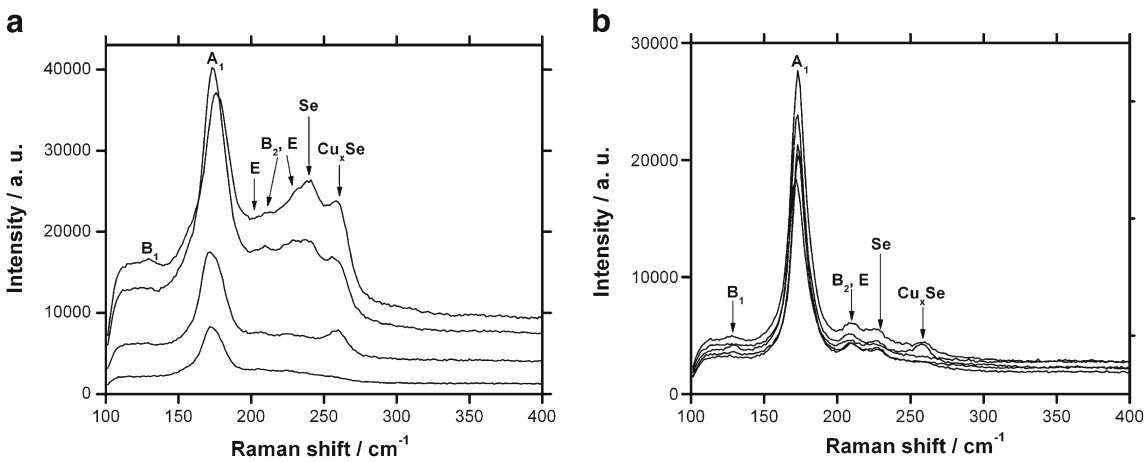

Fig. 7 Raman spectra of samples prepared by PuED with 90 pulses **a** as-deposited; **b** annealed at 500 °C in argon for 30 min

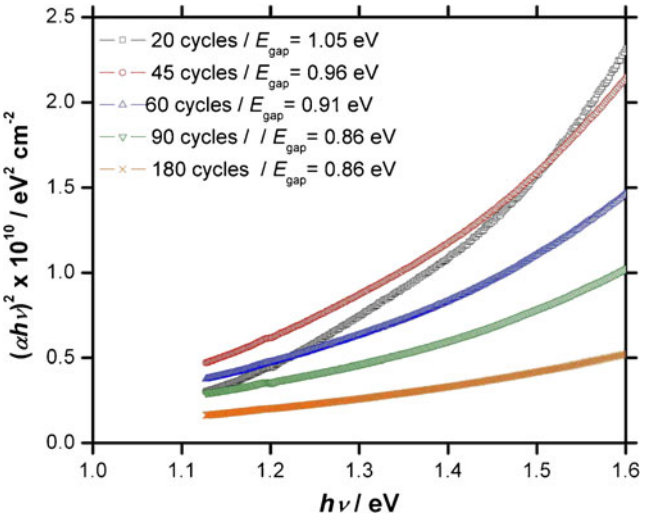

Fig. 8 Plots of $(\alpha h\nu)^2$ vs. $(h\nu)$ for annealed $CuInSe_2$ films. The films have been deposited using 20, 45, 60, 90, and 180 pulses

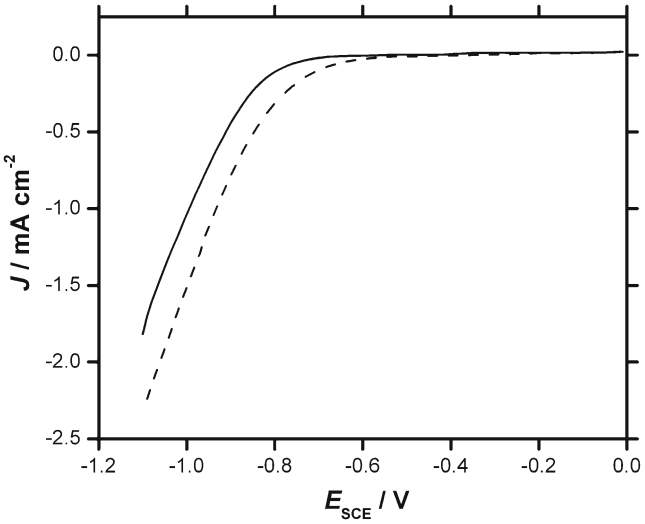

Fig. 10 I–V curve of $CuInSe_2$ film in contact with in 0.1 mol L^{-1} Na_2SO_4 solution in the dark (*solid curve*) and under simulated solar light (*dashed curve*). $CuInSe_2$ films were prepared by PuED and then annealed in argon

cycles were applied. The deposits were compared with others which were prepared applying a constant potential, during 400 to 3,600 s. Those films prepared using constant potential do not show any of the diffraction planes typical of the $CuInSe_2$ chalcopyrite phase, and they are mostly formed by binary compounds with indium and copper. After annealing, these films still present indium-rich phases like In_2Se_3 at short deposition times (900 s). At longer times (1,800 s), a ternary In-rich compound could be identified ($Cu_{0.39}In_{1.20}Se_2$) together with In_2O_3. These are probably formed during annealing due to the high concentration in indium that was revealed using EDS and Raman spectroscopy. Thus, −0.9 V_{SCE} does not seem to be a proper potential to obtain stoichiometric films in constant potential mode even after annealing the film.

In contrast, by pulsing the potential, and particularly after applying 90 or more pulses, broad signals of copper selenides and $CuInSe_2$ are present in the X-ray diffractogram. Diffraction peaks typical of the tetragonal $CuInSe_2$ structure are clearly seen after annealing with small residual signals of cupric selenide.

The composition of the sample is homogeneous, as demonstrated by Raman micromapping. Films prepared using a low number of cycles show blue-shifted vibration modes that can be attributed to residual stress or to a higher density of defects present in these films.

Using potential pulses, the presence of secondary phases in as-deposited samples can be greatly reduced. The presence of binary phases decreases when more pulses are applied, so that KCN etching can be minimized. The film morphology, homogeneity, and the degree of substrate coverage also improve when the potential is pulsed, particularly using 90 or 180 cycles.

Photoelectrochemical tests and current–voltage curves confirm p-type conduction and show higher photocurrents for samples prepared with pulsed potential. The high currents registered at the beginning of each step and the differences in the diffusion regime imposed by the two potential regimes could be responsible for the distinctive behavior of samples electrodeposited with pulsed or constant potential.

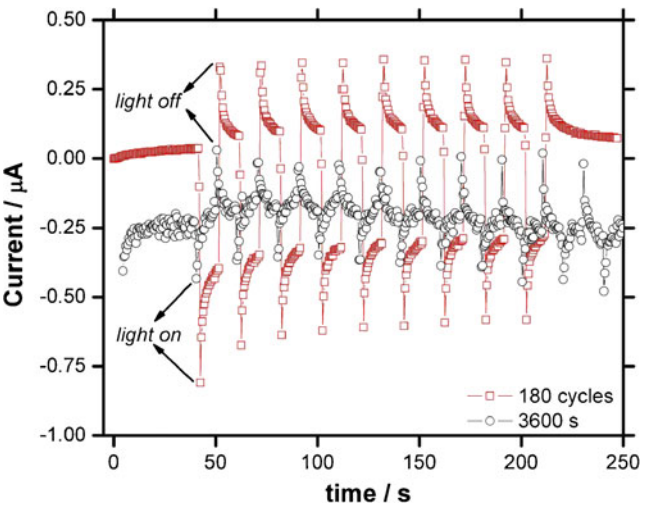

Fig. 9 Photocurrent response of annealed $CuInSe_2$ films immersed in 0.1 mol L^{-1} Na_2SO_4 solution, using chopped light (10 s on/10 s off). $CuInSe_2$ films were prepared by PuED with 180 pulses (*hollow squares*) and constant potential deposition during 3600 s (*hollow circles*)

Acknowledgments Financial support from *Consejo Nacional de Investigaciones Científicas y Técnicas* (CONICET), *Agencia Nacional de Promoción Científica y Tecnológica*, and *Universidad Nacional de Mar del Plata* (UNMdP) from Argentina is highly acknowledged. We kindly acknowledge BSc. Mariela Desimone for her assistance with GXRD measurements.

References

1. Lincot D, Guillemoles JF, Taunier S, Guimard D, Sicx-Kurdi J, Chaumont A, Roussel O, Ramdani O, Hubert C, Fauvarque JP, Bodereau N, Parissi L, Panheleux P, Fanouillere P, Naghavi N, Grand PP, Benfarah M, Mogensen P, Kerrec O (2004) Sol Energy 77(6):725–737
2. Chen HH, Kalu PN, Kalu EE (2010) J Solid State Electrochem 14 (6):1013–1020
3. Phok S, Rajaputra S, Singh VP (2007) Nanotechnology 18 (47):475601
4. Fu Y, Wei ZD, Chen SG, Li L, Feng YC, Wang YQ, Ma XL, Liao MJ, Shen PK, Jiang SP (2009) J Power Sources 189(2):982–987
5. Soga T (2006) Nanostructured materials for solar energy conversion. Elsevier, Amsterdam
6. Kemell M, Ritala M, Leskelá M (2005) Crit Rev Solid State Mater Sci 30(1):1–31
7. Mönig H, Fischer CH, Caballero R, Kaufmann CA, Allsop N, Gorgoi M, Klenk R, Schock HW, Lehmann S, Lux-Steiner MC, Lauermann I (2009) Acta Mater 57(12):3645–3651
8. Hibberd CJ, Chassaing E, Liu W, Mitzi DB, Lincot D, Tiwari AN (2010) Prog Photovoltaics Res Appl 18(6):434–452
9. Palacios-Padrós A, Caballero-Briones F, Sanz F (2010) Electrochem Commun 12(8):1025–1029
10. Guillemoles JF, Cowache P, Lusson A, Fezzaa K, Boisivon F, Vedel J, Lincot D (1996) J Appl Phys 79(9):7293–7302
11. Valdés MH, Vázquez M (2011) Electrochim Acta 56(19):6866–6873
12. Valdés M, Frontini MA, Vázquez M, Goossens A (2007) Appl Surf Sci 254((1 SPEC. ISS):303–307
13. Kang F, Ao J, Sun G, He Q, Sun Y (2009) J Alloys Compd 478(1–2):L25-L27
14. International Centre for Difraction Data (ICCD) (1998) Powder difraction file database. Newtown Square, EEUU
15. Chandrasekar MS, Pushpavanam M (2008) Electrochim Acta 53:3313–3322
16. Lide DR (ed) (1998) Handbook of chemistry and physics, 79th edition, CRC press, Boca Raton
17. Calixto E, Dobson KD, McCandless BE, Birkmire RW (2006) J Electrochem Soc 153(6):G521–G528
18. Whang TJ, Hsieh MT, Kao YC, Lee SJ (2009) Appl Surf Sci 255 (8):4600–4605
19. Araujo J, Ortíz R, López-Rivera A, Ortega JM, Montilla M, Alarcón D (2007) J Solid State Electrochem 11:407–412
20. Yang J, Jin Z, Li C, Wang W, Chai Y (2009) Electrochem Commun 11(3):711–714
21. Tang K, Künecke U, Oehlschläger F, Hölzing A, Schurr R, Hock R, Wellmann PW (2010) Sol Energy Mater Sol Cells 94(11):1875–1879
22. Ramdani O, Chassaing E, Canava B, Grand PP, Roussel O, Lamirand M, Rzepka E, Etcheberry A, Guillemoles JF, Lincot D, Kerrec O (2007) J Electrochem Soc 154(8):D383–D393
23. Chassaing E, Ramdani O, Grand PP, Guillemoles JF, Lincot D (2008) Phys Status Solidi C 5(11):3445–3448
24. Gouadec G, Colomban P (2007) Prog Crys Growth Charact Mater 53(1):1–56
25. Izquierdo-Roca V, Pérez-Rodríguez A, Romano-Rodríguez A, Morante JR, Alvarez-García J, Calvo-Barrio L, Bermudez V, Grand PP, Ramdani O, Parissi L, Kerrec O (2007) J Appl Phys 101(10):103517-103518
26. Chassaing E, Roussel O, Ramdani O, Grand PP, Canava B, Etcheberry A, Guillemoles JF, Lincot D (2007) ECS Trans 6:577–585
27. Roussel O, Ramdani O, Chassaing E, Grand PP, Lamirand M, Etcheberry A, Kerrec O, Guillemoles JF, Lincot D (2008) J Electrochem Soc 155(2):D141–D147
28. Rincón C, Wasim SM, Marín G, Delgado JM, Huntzinger JR, Zwick A, Galibert J (1998) Appl Phys Lett 73(4):441–443
29. Weszka J, Daniel P, Burian A, Burian AM, Nguyen AT (2000) J Non-Cryst Solids 265(1–2):98–104
30. Lyu DY, Lin TY, Chang TW, Lan SM, Yang TN, Chiang CC, Chen CL, Chiang HP (2010) J Alloys Compd 499(1):104–107
31. Ramdani O, Guillemoles JF, Lincot D, Grand PP, Chassaing E, Kerrec O, Rzepka E (2007) Thin Solid Films 515(15):5909–5912
32. Kang SH, Kim YK, Choi DS, Sung YE (2006) Electrochim Acta 51(21):4433–4438
33. Álvarez-García J, Barcones B, Pérez-Rodríguez A, Romano-Rodríguez A, Morante JR, Janotti A, Wei SH, Scheer R (2005) Phys Rev B: Condens Matter 71(5):1–9
34. Volobujeva O, Altosaar M, Raudoja J, Mellikov E, Grossberg M, Kaupmees L, Barvinschi P (2009) Sol Energy Mater Sol Cells 93 (1):11–14
35. Valdés M, Vázquez M, Goossens A (2008) Electrochim Acta 54 (2):524–529
36. Dale PJ, Samantilleke AP, Zoppi G, Forbes I, Peter LM (2008) J Phys D Appl Phys 41(8):085105
37. Akl AA, Afify HH (2008) Mater Res Bull 43(6):1539–1548
38. Edamura T, Muto J (1994) J Mater Sci Mater Electron 5(5):275–279
39. Sato N (1998) Electrochemistry at metal and semiconductor electrodes. Elsevier, Amsterdam